XMM–Newton observations of NGC 3268 in the Antlia Galaxy Cluster: characterization of a hidden group of galaxies at $z \approx 0.41$

I. D. Gargiulo,[1,4]★ F. García,[2,3,4,5] J. A. Combi,[2,3,4] J. P. Caso[1,2,4] and L. P. Bassino[1,2,4]

[1]*Instituto de Astrofísica de La Plata (CCT La Plata, CONICET, UNLP), Paseo del Bosque s/n, B1900FWA La Plata, Argentina*
[2]*Facultad de Ciencias Astronómicas y Geofísicas, Universidad Nacional de La Plata, Paseo del Bosque, B1900FWA La Plata, Argentina*
[3]*Instituto Argentino de Radioastronomía (CCT-La Plata, CONICET; CICPBA), C.C. No. 5, 1894 Villa Elisa, Argentina*
[4]*Consejo Nacional de Investigaciones Científicas y Técnicas, Rivadavia 1917, Ciudad Autónoma de Buenos Aires, C1033AAJ Buenos Aires, Argentina*
[5]*Laboratoire AIM (UMR 7158 CEA/DRF-CNRS-Université Paris Diderot), Irfu/Département d'Astrophysique, Centre de Saclay, F-91191 Gif-sur-Yvette, France*

ABSTRACT

We report on a detailed X-ray study of the extended emission of the intracluster medium (ICM) around NGC 3268 in the Antlia Cluster of galaxies, together with a characterization of an extended source in the field, namely a background cluster of galaxies at $z \approx 0.41$, which was previously accounted as an X-ray point source. The spectral properties of the extended emission of the gas present in Antlia were studied using data from the *XMM–Newton* satellite, complemented with optical images of Cerro Tololo Inter-American Observatory (CTIO) *Blanco* telescope, to attain for associations of the optical sources with the X-ray emission. The *XMM–Newton* observations show that the intracluster gas is concentrated in a region centred in one of the main galaxies of the cluster, NGC 3268. By means of a spatially resolved spectral analysis, we derived abundances of the ICM plasma. We found a wall-like feature in the north-east direction, where the gas is characterized by a lower temperature with respect to the rest of the ICM. Furthermore, using combined optical observations, we inferred the presence of an elliptical galaxy in the centre of the extended X-ray source considered as a background cluster, which favours this interpretation.

Key words: galaxies: clusters: individual: (ACO S636) – galaxies: clusters: intracluster medium – X-rays: galaxies: clusters.

1 INTRODUCTION

The Antlia Cluster, catalogued as ACO S636 (Abell, Corwin & Olowin 1989), is the third nearest cluster of galaxies ($d=$ 35.2 Mpc; Dirsch, Richtler & Bassino 2003). The central region of the cluster seems to be composed of two subgroups, focused around NGC 3268 and NGC 3258, two giant ellipticals (gEs) with similar luminosity. The northern group is dominated by NGC 3268, which is surrounded by three bright lenticulars. Despite the proximity to the projected distance, their membership to the same bound system has been reconsidered by Caso & Richtler (2015). The southern group is dominated by NGC 3258 and surrounded by two large lenticulars. The galaxy population of the Antlia Cluster was studied by Hopp & Materne (1985) and Ferguson & Sandage (1990, 1991), who found that the cluster hosts 420 galaxies. During the last decade, there was a renewed interest in the cluster and several observations in the optical range were carried out. Studies with deep images and follow-up spectroscopy allowed to confirm the membership of additional low-surface-brightness galaxies (Smith Castelli et al. 2008, 2012; Calderón et al. 2015). The globular cluster systems of both gEs were studied (Dirsch, Richtler & Bassino 2003; Harris et al. 2006; Bassino, Richtler & Dirsch 2008), and ultra-compact dwarfs were discovered around both galaxies. Recently, the properties of these objects were analysed by Caso et al. (2013, 2014).

In the X-ray domain, the Antlia Cluster was first studied by Pedersen, Yoshii & Sommer-Larsen (1997). They used observations performed by the *ASCA* satellite in the region surrounding NGC 3258 in order to determine the baryonic fraction of the group. They detected diffuse emission centred on the group and extending north-eastward beyond the field of view (FOV), towards NGC 3268. These authors performed a simultaneous fit of the two gas imaging spectrometry (GIS) cameras of a beta model to the surface brightness profile and found a value of $\beta = 0.6 \pm 0.2$ and a core radius of $r_{\rm c} = 156.8 \pm 70\,{\rm h}_{70}^{-1}$ kpc. Integrating the profile, they found a gas mass inside 336 ${\rm h}_{70}^{-1}$ kpc of $M_{\rm gas} = 1.8 \times 10^{12}\,{\rm h}_{70}^{-5/2}$ M⊙. They also extracted spectra for the three cameras in the instrument, and the simultaneous fit of the GIS cameras yielded a temperature of

★ E-mail: ignacio.gargiulo@gmail.com

$k_T = 1.90^{+0.21}_{-0.1}$ keV and a metal abundance of $Z = 0.11^{+0.15}_{-0.1}$ solar. Later on, Nakazawa et al. ([2000](#)) used observations of the *ASCA* satellite that include the region surrounding NGC 3268. They studied the extended emission of the intracluster gas and found first that the X-ray brightness profile showed two peaks, one almost coincident with NGC 3268 and another ∼5 arcmin to the west of NGC 3268. They were unable to conclude which of the peaks represented the real position of the minimum of the potential well due to limitations of the instrument. Hence, they had to use images from *ROSAT* PSPC archival data to unveil this issue. In these images, the peak to the west appeared like a point-like source, and they concluded that the only peak of diffuse emission was the one almost coincident with the position of NGC 3268. After extracting spectra of nine different regions around NGC 3268, they fitted a single-temperature model for all the regions and found that the cluster emission appears to be isothermal with a temperature of ∼2.0 keV and a metallicity of $Z = 0.35\,Z_{\odot}$. However, they found that adding a cool component that represents gas at roughly 1.0 keV yields a better fit to the spectra at low energies (∼1 keV). The luminosity share of the cool component that they found is ∼20 per cent of the total luminosity of the gas within $70\,h_{70}^{-1}$ kpc. Recently, Wong et al. ([2016](#)) studied *Suzaku* observations of the outskirts of Antlia out to $1.3\,R_{200}$ in the east direction, where the cluster seems to be in equilibrium. They used *Chandra* and *XMM–Newton* data to identify and exclude point-like sources of their analysis. They found that the extended emission to the west of NGC 3268 is likely a background cluster of galaxies, considering the spectral features of the source.

Hess et al. ([2015](#)) studied the substructure of the Antlia Cluster through HI observations of a vast region around NGC 3268 and detected several groups of galaxies that are in the process of infalling into the cluster centre. They concluded that the group of galaxies around NGC 3268 is the central structure of the cluster.

In this work, we analyse X-ray observations of the region around NGC 3268 in the Antlia Cluster obtained by the X-ray Multi-Mirror Mission (*XMM–Newton*) satellite. The intracluster medium (ICM) is spectroscopically analysed, and new features of the emission are discovered. In particular, we fully characterize an extended source of emission to the west of NGC 3268 and associate it to a hidden group or cluster of galaxies at $z \approx 0.41$.

The paper is organized as follows. In Section 2, we present the *XMM–Newton* observations and the data reduction as well as the Cerro Tololo Inter-American Observatory (CTIO) *Blanco* optical image. Optical data analysis, X-ray image, and spectral results for the extended emission of the Antlia ICM and the background cluster are presented in Section 3, and, finally, the discussion is presented in Section 4. In this work, we use the cosmological parameters derived by Planck Collaboration XIII ([2016](#); $\Omega_\Lambda = 0.691$, $\Omega_m = 0.3099$ and $h = 0.67$).

2 DATA REDUCTION AND ANALYSIS

2.1 X-ray data

SASThe group of galaxies centred around NGC 3268 in the Antlia Cluster was observed with the European Photon Imaging Camera (EPIC) on board the *XMM–Newton* X-ray observatory, using the PN and MOS1/2 cameras. Three different observations were carried out during 2010 March, 2012 December, and 2013 January. The study presented in this paper is based on the two data sets with longer exposure, which encompasses more than 100 ks each. The XMM data were analysed with the XMM Science Analysis System ()

Table 1. *XMM–Newton* observations of the Antlia cluster.

Obs-id	0691950101	0691950201
Date	2013 January 5	2012 December 26
Exposure (ks)	83.9/99.7/99.7	90.6/108.4/108.5
GTI (ks)	68.6/78.4/83.8	90.5/107.9/108.1

Note. The two observations were taken from the *XMM–Newton* archive. Exposure and GTIs are indicated for PN/MOS1/2 cameras, respectively.

version 17.0 and the latest calibrations available in 2017 June. To exclude background flares, which can affect the observations, we followed the standard procedure to produce Good Time Interval (GTIs) files, using the SAS task ESPFILT. We list detailed information of the observations in Table [1](#).

We produced images in different energy bands by performing a double background subtraction to clean both the particle and X-ray background contaminations. We used Filter Wheel Closed and Blank Sky files available at *XMM ESAC* web pages.[1] Medium filters were used in each camera for these observations. Following the procedure described in Miceli et al. ([2017](#)), we created background-subtracted images for each camera, correcting for vignetting effects and exposure maps produced for each energy band. Finally, we mosaicked and adaptively smoothed the images using the SAS tasks EMOSAIC and ASMOOTH.

In the left-hand panel of Fig.[1](#), we show the resulting composite X-ray image obtained by combining the three EPIC exposures using a spatial binning of 4 arcsec. The soft band (0.3−1.0 keV) is shown in red, the medium band (1.0−2.0 keV) in green, and the hard (2.0−5.0 keV) band in blue.

2.2 Optical data

In order to investigate the nature of the two emission peaks of the ICM, we also use wide-field (36 arcmin × 36 arcmin) images in *R* Kron-Cousins and *C* Washington filters, obtained with the MOSAIC camera mounted on the 4-m *Blanco* telescope from CTIO. The observations were carried out during 2001 April 4–5. Refer to Dirsch et al. ([2003](#)) for further information about these data.

In Fig. [1](#) (right-hand panel), we show the optical image with the usual orientation (north is up, east to the left). The square with dashed lines highlights the *XMM–Newton* field, and the square with solid lines highlights the region of the Antlia Cluster studied in this paper.

3 RESULTS

3.1 X-ray images

The FOV of the detectors is about 30 arcmin across. The white rectangle with solid lines in Fig. [1](#) indicates the region studied in detail in this work. The region contains the emission of the ICM around NGC 3268.

We found that the X-ray emission of the diffuse gas has two peaks (see the left-hand panel of Fig. [1](#)), as first noted by Nakazawa et al. ([2000](#)). One of the maximums of emission is located at the position of NGC 3268 and the other at ∼5 arcmin to the west of NGC 3268. If we focus on the strong emission region of the second peak (SP) of the ICM in the optical image, we can see that no obvious optical

---

[1] https://www.cosmos.esa.int/web/xmm-newton/filter-closed   http://xmm-tools.cosmos.esa.int/external/xmm_calibration/background/bs_repository/blanksky_all.html
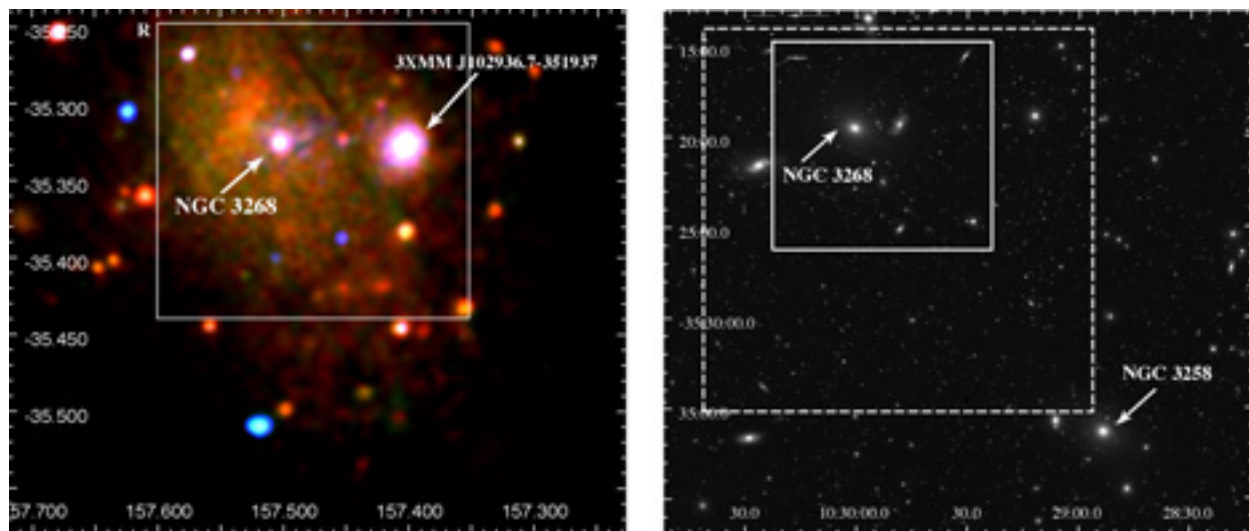
Figure 1. Left: *XMM–Newton* MOS1, MOS2, and PN combined image of a region around NGC 3268 in the Antlia Galaxy Cluster, with a size of 21.5 arcmin × 20.5 arcmin. The image is a combination of three X-ray energy bands: soft (0.3−1.0 keV) in red, medium (1.0−2.0 keV) in green, and hard (2.0−5.0 keV) in blue. R is the region that we studied in this work. Right: Optical field of the central region of Antlia observed with the *Blanco* telescope (CTIO) in the *R*-band (Dirsch et al. 2003). Highlighted in dashed white lines is the field of the X-ray observations delimited in the left-hand panel and with a solid line the region under consideration in this article.

counterpart is present. Only a weak point-like detection lies in the middle of the emission region, but a search through the NED and SIMBAD data bases in the coordinates of the object (α: 10:29:37, δ: −35:19:36.5, J2000) has thrown negative results. The extended source was detected in the sixth data release of the *XMM–Newton* Serendipitous Source Catalogue (3XMM-DR6) and named 3XMM J102936.7-351937. Hereafter, we shall name this region of emission as the SP. The point of maximum emission of this extended X-ray source is offset with respect to the dim object detected in the optical range by 16 arcsec. It was detected in 3XMM-DR6 as a point-like source and named 3XMM J102936.4-351922.

In Fig. 2, we show X-ray images of region R in the three narrow bands defined separately. Superimposed in yellow are the contours of radio emission, obtained from the Sydney University Molonglo Sky Survey (SUMSS; Mauch et al. 2003) source catalogue web page.[2] Contours were obtained from the downloaded images. There are indications that the distribution of the gas is elongated towards the other luminous galaxy of the cluster, NGC 3258, located in the south-west of NGC 3268 (see also the left-hand panel of Fig.1). In the soft energy range (left-hand panel of Fig. 2), the emission is extended in the ICM and is more intense in the two peaks of emission. We can see a notorious wall-like feature to the east of NGC 3268, which is only visible in the soft X-ray band. At medium energies (middle panel of Fig. 2), the ICM shows an even emission, but more concentrated in the central regions of the gas distribution. The SP of extended emission to the west of NGC 3268 shows more emission in this range than that in the peak around NGC 3268. At hard energies (right-hand panel of Fig. 2), this difference becomes more notorious. This suggests that the SP of the emission may not be just a thermal emitting source or that the temperature is higher in this region.

3.2 Optical images

Visual inspection of Fig. 1 fails to reveal the presence of a luminous source in the optical range located at the centre of the SP of emission in the X-ray band. Fig. 3 shows a composite image from *R* and *C* filters. The field corresponds to 2 arcmin × 2 arcmin. The white circle is centred on the SP of emission, and its radius of 0.5 arcmin barely spans the extension of the X-ray emission. In this deeper image, we can recognize that several extended sources are contained in the region of emission of the SP, including one very close to its centre. We analysed the surface brightness profiles of several point sources and the one corresponding to the extended object in the centre. While the points sources presented a typical full width at half maximum (FWHM) of ≈4 pixels, the latter object had FWHM ≈ 6, which is equivalent to 1.6 arcsec according to the image scale of 0.27 arcsec pixel^{-1}. We used the software ISHAPE (Larsen 1999) in order to fit the luminosity profile of the sources located in the SP region. This software calculates structural parameters of marginally resolved sources by fitting to each source the convolution between the PSF of the image and an analytical profile selected by the user. In order to produce accurate results, the fitted sources should have signal-to-noise (S/N) ratio ≈ 50, thus limiting our analysis to the bright source at SP centre. Previously to fitting the galaxy with ISHAPE, we subtracted a point source located at ∼3 arcsec in order to avoid contamination. This procedure was repeated iteratively in order to minimize the residuals. We applied Sérsic models (Sersic 1968), which have proven to accurately represent the surface brightness profiles of galaxies. As a first approach, we fixed the Sérsic index at different values within the usual range and fitted the profile. Afterwards, we fitted the profile considering the Sérsic index as a free parameter and obtained a value of $n = 2.2$. In all the cases, the initial fitting radius was 12 pixels, similar to the PSF radius. The fitting process was run iteratively in each case, varying the fitting radius as twice the effective radius in the previous step. This criterion is usually used in fitting photometry for unresolved or marginally resolved sources in nearby galaxies. The iteration was finished when results become stable. In Table 2,
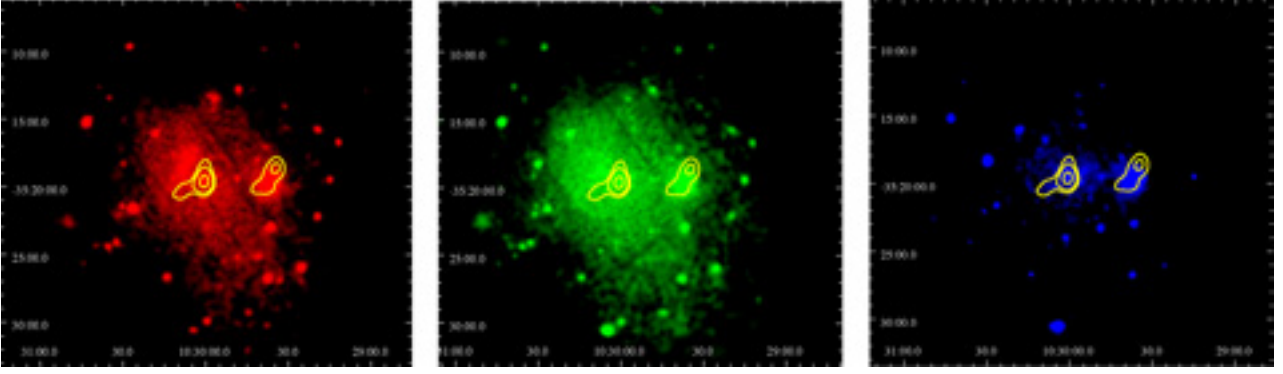
Figure 2. *XMM–Newton* X-ray images of the same region around NGC 3268 as in Fig. 1. Overlapping yellow contours represent the radio emission extracted from SUMSS. Left: soft X-rays (0.3−1.0 keV). Middle: medium X-rays (1.0−2.0 keV). Right: hard X-rays (2.0−5.0 keV).
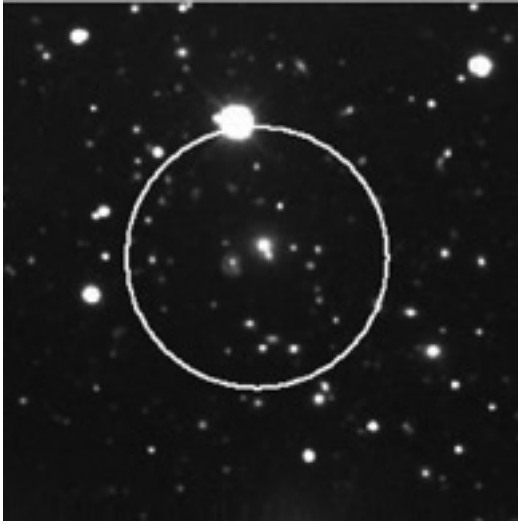

Figure 3. Combined image in *C* and *R* filters of the region around the SP of diffuse emission of the Antlia Cluster ICM. The image size is 2 arcmin × 2 arcmin. The white circle indicates the extension of the aforementioned X-ray emission. A non-point-like optical source lies in the middle of the emission.

Table 2. Parameters of the Sérsic model fits to the extended optical counterpart in the centre of 3XMM J102936.7-351937, with a fixed Sérsic index. Sérsic index, effective radius, ellipticity, and reduced chi-squared statistic are listed for five different fits.

n_{sersic}	R_{eff} (pixels)	R_{eff} (arcsec)	ϵ	χ^2_ν
1	3.4 ± 0.2	0.93 ± 0.05	0.09 ± 0.03	6.1
2	5.2 ± 0.2	1.40 ± 0.05	0.08 ± 0.03	2.4
3	9.0 ± 0.1	2.4 ± 0.3	0.08 ± 0.02	1.7
4	13.7 ± 0.1	3.7 ± 0.3	0.11 ± 0.02	2
2.2	6.5 ± 0.1	1.8 ± 0.3	0.09 ± 0.02	2.5

Note. The value $n = 2.2$ was obtained leaving the Sérsic index as a free parameter in the fit.

we show the corresponding Sérsic index for each fit, together with the effective radius (R_{eff}) in pixels and arcsec, the ellipticity, and the reduced χ^2_ν produced by the fit. The best result was obtained with $n = 3$, smaller than usual values for gEs but in agreement with cluster galaxies at $z \approx 1$ (e.g. Sweet et al. 2017). This corresponds to $R_{\mathrm{eff}} \approx 13$ kpc, similar to those from the more extended galaxies at similar
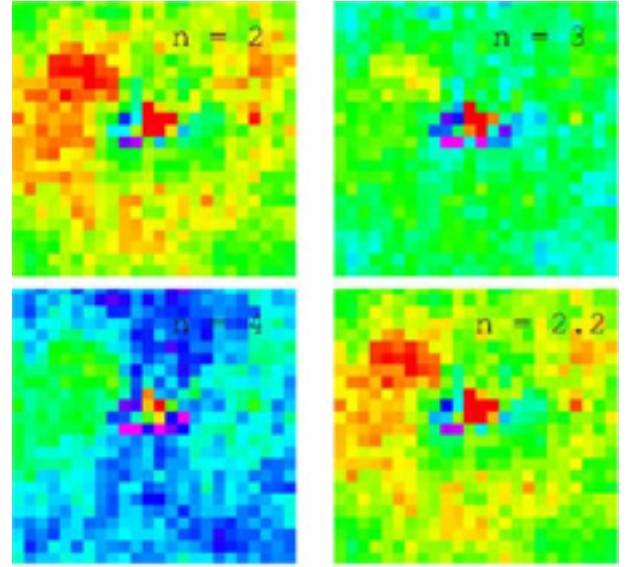

Figure 4. Residuals in the image of the SP of emission when different Sérsic profile models are subtracted. From top left to bottom right, models with Sérsic indexes $n = 2$, $n = 3$, $n = 4.4$, and $n = 2.2$ are shown. The palette colours spread from blue to red, representing the counts in the residual image from 9100 to 9550. Background counts correspond to green.

z (e.g. Jørgensen & Chiboucas 2013; Oldham, Houghton & Davies 2017; see Section 3.4.2 where the background cluster redshift is determined). Depending on the assumed index for the size evolution relation (e.g. Oldham et al. 2017; Sweet et al. 2017), it implies an $R_{\mathrm{eff}} \approx 15−20$ kpc, at $z = 0$, in the range of massive galaxies in the local Universe (Kormendy et al. 2009; Calderón et al. 2015). Fig. 4 shows the residuals obtained for the fitted profiles. The palette colours spread from blue to red, centred on the background level (≈ 9325 counts), which corresponds to green. In all the cases, the central pixels seem to be underestimated. Residuals from $n = 2$ and $n = 2.2$ present a ring-like structure, due to the profile behaviour at the outskirts. This is also present in the case of $n = 1$, which is not shown in the figure.

3.3 X-ray spectra

In this section, we present the X-ray spectral analysis of the regions of interest indicated with circles and ellipses in Fig. 5. We use the HEASARC XSPEC package (v12.9.1, from HEASOFT v20; Arnaud 1996)
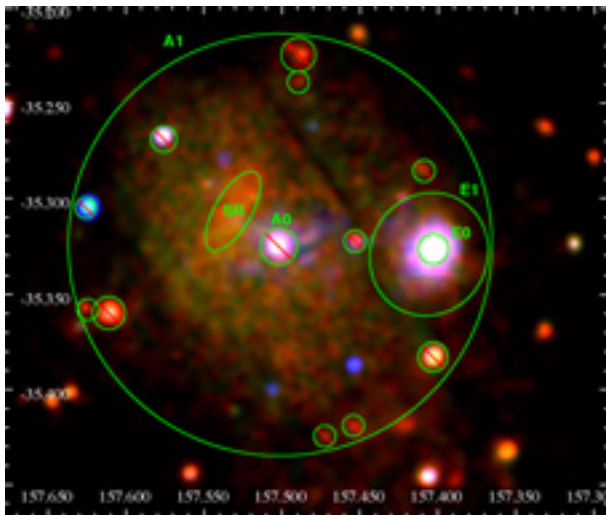
Figure 5. X-ray observations of the ICM around NGC 3268. Zoomed region R from Fig. 1. Enclosed with green circles and marked as A0 and E0 are the two peaks of emission of the ICM. A0 is almost coincident with one of the central galaxies of the Antlia Cluster, NGC 3268. E0 encloses the maximum emission of the SP of extended emission. Surrounding A0 is a wider annulus centred in the peak of emission and named as region A1. Region E0 is surrounded with an elliptical region encompassing the emission of this extended source. Region SR delimits the emission of a wall-like soft X-ray source. Emission of point-like sources is excluded from the analysis.

to perform a standard spectral analysis of the sources in order to fit spectral models to the data. Spectra were obtained using the evselect SAS task. A source spectrum was obtained together with a background spectrum. Regions around NGC 3268 and the SP of the extended emission share the same background, obtained in the more external parts of the FOV (see Subsection 3.4.1). Ancillary Response Files (ARFs) and Redistribution Matrix Files (RMFs) were produced using the ARFGEN and RMFGEN SAS tasks, respectively. The input of all the detectors was fitted simultaneously with the same model. The bad pixels were excluded and only channels in the range where the sources have emission were considered. All the chemical abundances (A) are referred to the solar abundances of Anders & Grevesse (1989).

3.4 Diffuse emission of the ICM

The crucial features of the X-ray extended emission of the Antlia Cluster in the region around NGC 3268 are the wall-like emission region close to the east of NGC 3268 and the ICM emission centred in NGC 3268. In this section, we analyse the spectra of these regions. We postpone the analysis of the SP of emission until the next section.

First, we analyse the centre of emission of the ICM. Fig. 5 shows a zoomed image of the ICM of the region of the Antlia Cluster surrounding NGC 3268, tagged as R in Fig. 1. We define a pair of regions centred in the first peak, almost coincident with NGC 3268, and fit models to the background-subtracted spectra obtained from the *XMM–Newton* EPIC MOS1/2 and PN data. The selected regions consist of circles enclosing the central emission (tagged as A0) and an annulus at a larger radius from the centre to characterize the temperature and detailed abundances of the ICM surrounding A0 (tagged as A1). We also study the spectral properties of an elliptical region surrounding the wall-like feature to the east of NGC 3268 (tagged as SR). Point-like sources were removed from the data as indicated in the figure.

After several tests, the best fit for region A1 was computed using a thermal emission model in equilibrium ionization APEC (Smith et al. 2001), widely used in the literature, and modified by an absorption model TBabs. The APEC model has as parameters the temperature of the emitting gas, its abundance, the redshift of the source, and the normalization factor. The version VAPEC adds the individual abundances. The TBabs model uses the cross-sections from Balucinska-Church & McCammon (1992). The only free parameter of this model is the hydrogen column density N_H. In the case of the galactic emission of NGC 3268, in the region A0, we found that the APEC model modified by the absorption model TBabs was not sufficient to fit the counts at higher energies, so we added a power law. As a consequence, the more energetic part of the spectrum is better reproduced and the overall fit results are more accurate. The free parameter of the power law is the photon index Γ and its normalization.

In previous studies, a redshift $z = 0.0087$ has been estimated for the Antlia Cluster (Nakazawa et al. 2000). We assume that the thermal emission of the hot gas surrounding NGC 3268 is responsible for the extended emission within region A1, so we fixed the redshift parameter. We also fixed the column density parameter of the TBabs model to the average value obtained for the direction of a cone of 1 deg of diameter with centre in NGC 3268, estimated in the HEASARC N_H tool that uses the Leiden/Argentine/Bonn HI survey (Kalberla et al. 2005), to determine the column density in a given direction of the sky. The X-ray parameters of the best fit to the diffuse emission spectra for two regions A0 and A1 are presented in Tables 3 and 4, respectively.

Since the PN spectrum of the extended emission of region A1 above 3.0 keV is dominated by the background, we did not include it in the analysis to maximize the S/N ratio. We also excluded the $1.7-1.8$ keV energy range in MOS data to avoid uncertainties introduced by the presence of a 1.75 keV Si-Kα line at the MOS central chips. We verified that our best-fitting models did not change significantly by adding the data in that energy range. While the uncertainty of the best-fitting parameters increased, the best-fitting parameters were always compatible within the errors. Fig. 6 shows the spectra of the fitted regions.

The residuals in all the cases are almost symmetrical and within reasonable values. For each region, we compute the total fluxes in the soft (0.3–1.3 keV), medium (1.3–3.0 keV), hard (3.0–5.5 keV), and total (0.3–5.5 keV) X-ray bands. We do not take into account the absorption because the value of the column's density obtained for the Antlia Cluster is too low to affect the results strongly. We performed a detailed chemical analysis of the ICM around NGC 3268. The iron line complex is ubiquitous in the regions around NGC 3268. The fitted values of metallicity in region A0 indicate that the ICM is enriched in oxygen and silicon and that the iron abundance is lower than abundances of other elements. On the other side, the fitted values of metallicity in region A1 show an overenrichment of oxygen, silicon, and sulphur while iron has a relative higher abundance than other elements. The temperature of 1.8 keV in region A1 is consistent within the errors with the previous results (Nakazawa et al. 2000). On the other hand, the temperature obtained for region A0 is lower than the results obtained in previous studies, when only a thermal origin was assumed for the emission of the cluster centre. In previous analysis, it was concluded that Antlia has not a cool core (CC), although the temperature drop could indicate the contrary. However, temperature drop at the centre of clusters (Maughan et al. 2012) is not a conclusive estimator of CC in clusters. We refer the reader to Section 3.5, where we address this issue specifically.

Table 3. Spectral parameters of the X-ray emission of the central region around NGC 3268, named A0.

Model and parameters	A0 region
TBabs∗(VAPEC+PO)	
TBabs	
N_H (10^{22} cm^{-2})	6.46×10^{-2}
VAPEC	
k_T (keV)	$1.32^{+0.01}_{-0.02}$
He, C, N, Ne, Mg, Al, Ar, Ca, Ni	$0.27^{+0.1}_{-0.1}$
O	$0.42^{+0.12}_{-0.11}$
Si	$0.32^{+0.06}_{-0.06}$
S	$0.28^{+0.1}_{-0.01}$
Fe	$0.13^{+0.01}_{-0.01}$
Norm (10^{-4})	$1.57^{+0.13}_{-0.13}$
Power law	
Γ	$1.35^{+0.00}_{-0.00}$
Norm (10^{-4})	$0.10^{+0.005}_{-0.005}$
χ^2_ν /degrees of freedom	0.91/869
Flux (0.3−1.3keV)	$6.24^{+0.06}_{-0.06}$
Flux (1.3−3.0keV)	$5.25^{+0.07}_{-0.07}$
Flux (3.0−5.5keV)	$3.08^{+0.07}_{-0.07}$
Total flux (0.3−5.5keV)	$14.58^{+0.14}_{-0.14}$

Notes. Normalization is defined as $10^{-14}/4\pi D^2 \times \int n_H n_e \, dV$, where D is distance (cm), n_H is the hydrogen density (cm^{-3}), n_e is the electron density (cm^{-3}), and V is the volume (cm^3). Fluxes are given in units of 10^{-14} erg cm^{-2} s^{-1} and are not absorption-corrected. Error values are given as 90 per cent confidence level for every single parameter. The redshift value in the model was fixed in $z = 0.0087$. The metal abundances are given relative to the solar abundance calculated by Anders & Grevesse (1989). Abundances parameters of He, C, N, Ne, Mg, Al, Ar, Ca, and Ni were tied because the spectral features do not constraint those abundances satisfactorily.

Table 4. Spectral parameters of the diffuse X-ray emission of the region around NGC 3268, named A1.

Model and parameters	A1 region
TBabs∗VAPEC	
TBabs	
N_H (10^{22} cm^{-2})	6.46×10^{-2}
VAPEC	
k_T (keV)	$1.8^{+0.02}_{-0.02}$
He, C, N, Ne, Mg, Al, Ar, Ca, Ni	$0.1^{+0.03}_{-0.03}$
O	$0.2^{+0.04}_{-0.03}$
Si	$0.31^{+0.02}_{-0.02}$
S	$0.47^{+0.03}_{-0.03}$
Fe	$0.17^{+0.01}_{-0.01}$
Norm (10^{-4})	$1.0^{+0.23}_{-0.23}$
χ^2_ν /degrees of freedom	1.32/1759
Flux (0.3−1.3keV)	$266.87^{+0.98}_{-0.98}$
Flux (1.3−3.0keV)	$234.83^{+1.22}_{-1.22}$
Total flux (0.3−3.0keV)	$501.71^{+1.67}_{-1.67}$

Notes. Same as in Table 3.
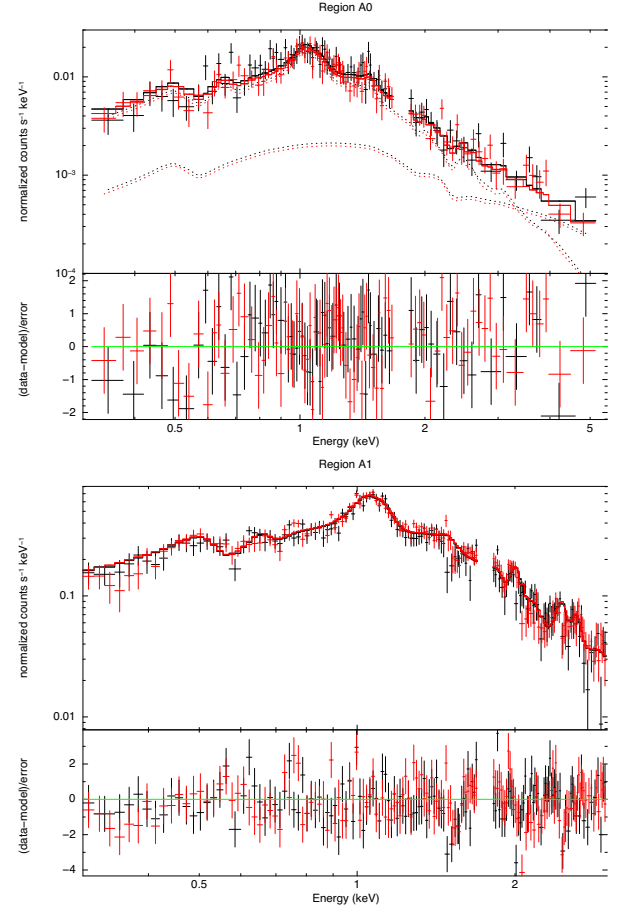
Figure 6. *XMM–Newton* spectra of selected regions around NGC 3268 (Fig. 5). Red and black symbols represent the normalized counts of MOS1/2 cameras obtained in one of the observations used in this work (Obs-id: 0691950101, see Section 2.1). Lower panels are the χ^2_ν fit residuals. A0: Dotted lines indicate individual contributions of each TBAbs∗VAPEC model and power-law model for the two cameras. Solid lines indicate the sum of the model components (see Table 3).

Besides the central regions of the cluster around NGC 3268, we took the spectra of a wall-like region that is seen in the soft energy band image shown in Section 3.1 and tagged as SR in Fig. 5. Our best fit to the data is a combination of two plasma models TBAbs∗(VAPEC+APEC), and the best-fitting parameters are listed in Table 5. The spectral analysis of the SR region shows that two different components coexist. One of the components shows a temperature of ∼0.61 keV, which is substantially lower than the temperature obtained for the best-fitting model in region A1 (1.8 keV). The other plasma best-fitting model returns a temperature of 1.61 keV, closer to the gas temperature measured for region A1. In Fig. 7, we show the spectrum of the SR region. Dotted lines indicate the contribution of the two different plasma models. We can see that the plasma model with lower fitting temperature helps to recover a bump in the spectrum in the range 0.7–0.9 keV.

3.4.1 Background treatment

The emission of the Antlia ICM is present in the whole FOV of *XMM–Newton*, together with the X-ray background emission. Therefore, some considerations about the background treatment in the spectral fitting are needed. We show in Fig. 8 two different back-

**Table 5.** Spectral parameters of the gas wall feature named as SR.

| Model and parameters	SR region
TBabs∗(VAPEC+APEC)	
TBabs	
N_H (10^{22} cm^{-2})	6.46×10^{-2}
VAPEC	
k_T (keV)	$1.61^{+0.03}_{-0.03}$
He, C, N, Ne, Mg, Al, Ar, Ca, Ni	$0.32^{+0.16}_{-0.10}$
O	$0.37^{+0.12}_{-0.10}$
Si	$0.32^{+0.09}_{-0.05}$
S	$0.34^{+0.11}_{-0.08}$
Fe	$0.19^{+0.03}_{-0.02}$
Norm (10^{-4})	$2.61^{+0.23}_{-0.34}$
APEC	
k_T (keV)	$0.61^{+0.04}_{-0.04}$
A ($A_\odot$)	$1.26^{+0.9}_{-1.}$
Norm (10^{-4})	$0.57^{+0.2}_{-0.4}$
χ^2_ν /degrees of freedom	0.99/1051
Flux (0.3−1.3keV)	$10.43^{+0.08}_{-0.07}$
Flux (1.3−3.0keV)	$7.05^{+0.09}_{-0.09}$
Total flux (0.3−Max keV)	$17.48^{+0.13}_{-0.15}$

Notes. Same as in Table 3.
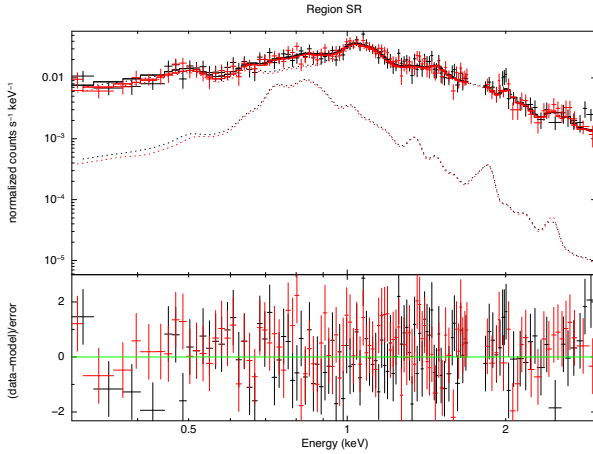
Figure 7. *XMM–Newton* spectra of region tagged as SR in Fig. 5. Red and black symbols represent the normalized counts of MOS1/2 cameras obtained in one of the observations used in this work (Obs-id: 0691950101, Section 2.1). Lower panels are the χ^2_ν fit residuals. Solid lines represent the sum of the contributions of different components of the model. Dotted lines are the individual contributions of the model components.

ground regions that we tested. Spectral fitting using alternatively one region or the other resulted in fully compatible best-fitting parameter values. In Fig. 9, we show the source spectrum of region A1 and the spectra of the two backgrounds. We can see that the background spectra are significantly different from the thermal emission of the cluster plasma but consistent between each other. Both background spectra are essentially formed by a power law plus certain specific emission lines originated in the detectors (as the strong Al-Kα line). To avoid possible issues arising from the 1.75 keV Si-Kα line present at the central MOS chips (and absent in the outer ones), we ignored the 1.7–1.8 keV energy range when fitting MOS spectra. Despite these emission line features, the intensity of the emission
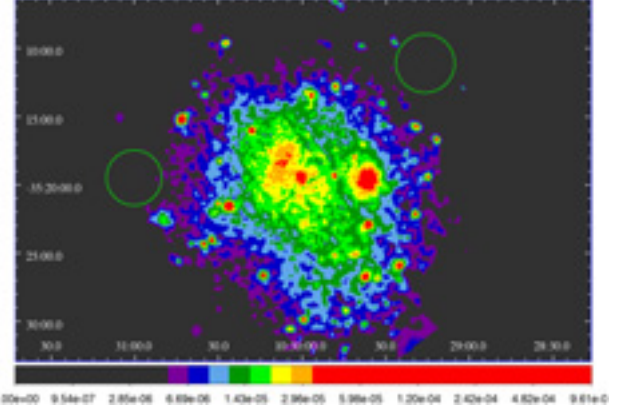
Figure 8. Highlighted with green circles two different selected background regions in the most external region of the FOV are shown. We tested the consistency of the results shown in the paper using both background regions.
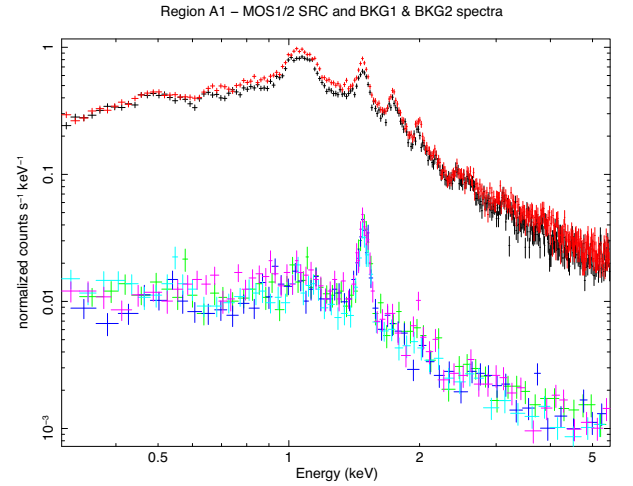
Figure 9. Red and black symbols represent the normalized counts of MOS1/2 cameras obtained in this work for region A1. Cyan, blue, green, and pink symbols are the normalized counts in both background regions.

in the region of the selected backgrounds is less than 10 per cent of that of the extended source.

3.4.2 Background cluster of galaxies

We consider here the spectral analysis for the two elliptical regions around the SP of emission, tagged as E0 and E1 in Fig. 5. The Antlia contribution was modelled with the same absorbed thermal plasma of the previous section. In both regions E0 and E1, we had to fit the data of the PN camera up to 3 keV, because, as a result of the sensitivity of the camera, the signal of the data in that range of energy started to compete with the signal of the background. In the case of E0, we determined the overall abundance through a VAPEC model, while in E1, we fitted the individual abundances to characterize the ICM of the cluster. Results of the spectral fit can be found in Tables 6 and 7.

The spectrum of the external region of the SP of emission (E1) presents a strong emission line at ~4.7 keV. Fig. 11 shows a more detailed view of the fitted line. Inspection in the AtomDB web data base reveals that there is no such strong line of emission around that energy. Now, if we consider that the SP of emission can be the

Table 6. Spectral parameters of the emission of the central region of the SP, named E0.

Model and parameters	E0 region
TBabs∗(APEC+APEC)	
TBabs	
N_H (10^{22} cm^{-2})	6.46×10^{-2}
APEC	
k_T (keV)	$2.06^{+0.39}_{-0.36}$
A (A$_\odot$)	$0.19^{+0.15}_{-0.06}$
Norm (10^{-4})	$0.67^{+0.29}_{-0.34}$
APEC	
k_T (keV)	$6.51^{+1.21}_{-0.97}$
A (A$_\odot$)	$0.60^{+0.33}_{-0.19}$
z	$0.422^{+0.006}_{-0.003}$
Norm (10^{-4})	$1.69^{+0.5}_{-0.5}$
χ^2_ν /degrees of freedom	0.98/704
Flux (0.3−1.3keV)	$8.40^{+0.1}_{-0.1}$
Flux (1.3−3.0keV)	$6.88^{+0.09}_{-0.08}$
Flux (3.0−5.5keV)	$5.04^{+0.17}_{-0.18}$
Total flux (0.3−5.5keV)	$20.32^{+0.26}_{-0.24}$

Notes. Normalization is defined as $10^{-14}/4\pi D^2 \times \int n_H n_e\,dV$, where D is distance (cm), n_H is the hydrogen density (cm^{-3}), n_e is the electron density (cm^{-3}), and V is the volume (cm^3). Fluxes are given in units of 10^{-14} erg cm^{-2} s^{-1} and are not absorption-corrected. Error values are given as the 90 per cent confidence level for every single parameter. The redshift parameter in the APEC model corresponding to the Antlia ICM was fixed in $z = 0.0087$. The metal abundance A is given relative to the solar abundance calculated by Anders & Grevesse (1989).

Table 7. Spectral parameters of the extended emission of the SP, named E1.

| Model and parameters	E1 region
TBabs∗(VAPEC+APEC)	
TBabs	
N_H (10^{22} cm^{-2})	6.46×10^{-2}
APEC	
k_T (keV)	$1.70^{+0.06}_{-0.03}$
He, C, N, Ne, Mg, Al, Ar, Ca, Ni	$0.31^{+0.15}_{-0.06}$
O	$0.56^{+0.44}_{-0.11}$
Si	$0.23^{+0.13}_{-0.06}$
S	$0.39^{+0.36}_{-0.09}$
Fe	$0.16^{+0.15}_{-0.02}$
Norm (10^{-4})	$5.11^{+1.27}_{-3.43}$
APEC	
k_T (keV)	$4.18^{+0.57}_{-0.80}$
A (A$_\odot$)	$0.26^{+0.11}_{-0.13}$
z	$0.413^{+0.005}_{-0.005}$
Norm (10^{-4})	$8.1^{+3.47}_{-1.37}$
χ^2_ν /degrees of freedom	1.10/1659
Flux (0.3−1.3keV)	$47.85^{+0.03}_{-0.03}$
Flux (1.3−3.0keV)	$32.51^{+0.03}_{-0.03}$
Flux (3.0−5.5keV)	$16.70^{+0.14}_{-0.84}$
Total flux (0.3−5.5keV)	$97.05^{+0.05}_{-0.04}$

Notes. Same as in Table 6.
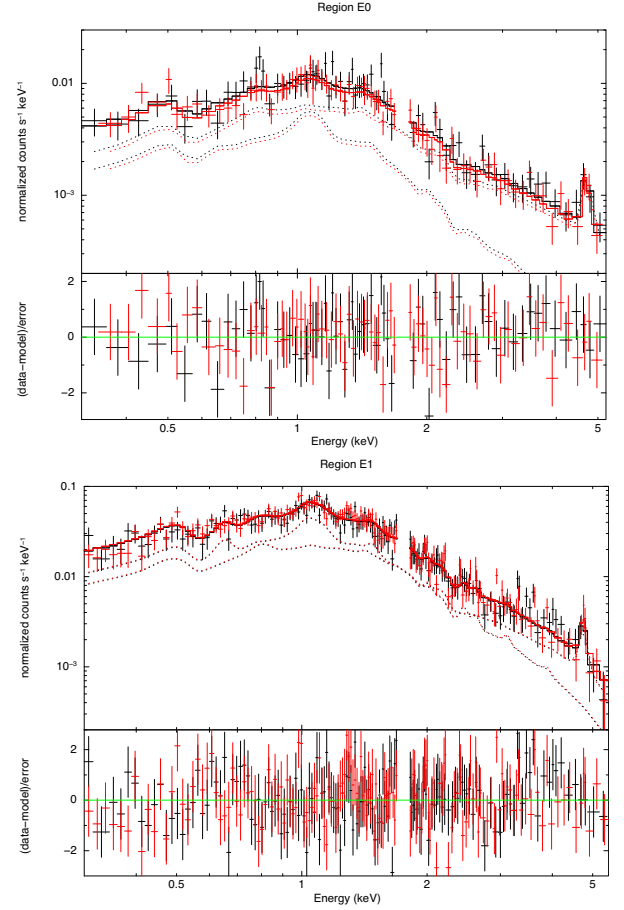
Figure 10. *XMM–Newton* spectra of selected regions enclosing the background cluster (Fig. 5). Red and black symbols represent the normalized counts of MOS1/2 cameras obtained in one of the observations used in this work (Obs-id: 0691950101, Section2.1). Solid lines represent the sum of the contributions of different components of the model. Dotted lines are the individual contributions of the model components.

extended emission of the hot gas of a group or cluster of galaxies in the background, the adjusted line in the spectrum would be redshifted. We tested this hypothesis by leaving the redshift parameter free in the additional APEC model in both regions E0 and E1. The result for the redshift parameter in our fits reveals that the X-ray emission of the SP corresponds to an object located at a redshift of $z \sim 0.41$, where the emission line detected at ~4.7 keV corresponds to a redshifted Fe-Kα line. Solid lines following the data in Fig.10 are the sum of the contributions of the model components, and dotted lines indicate each individual contribution. We can see that the first plasma model representing the Antlia emission is necessary to account for the iron bump near 1 keV, while the second plasma models adjust the more energetic part of the spectrum, where a redshifted iron line is present.

3.5 Does Antlia have a weak cool core?

Hudson et al. (2010) studied 16 different CC estimators in a sample of 64 clusters (Reiprich & Böhringer 2002) and found that cooling time (t_{cool}; Edge, Stewart & Fabian 1992; Mittal et al. 2009) and entropy (Cavagnolo et al. 2009) are the two CC estimators that show the most clear bimodality in their distribution. Therefore, they claim that t_{cool} is the best parameter to determine the existence
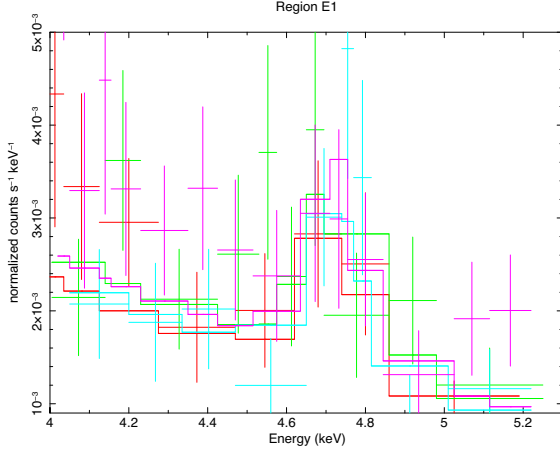
Figure 11. *XMM–Newton* zoomed region of the spectra of region E1 around the iron line at $\approx$4.7 keV.

Figure 12. Normalized surface brightness profile of the Antlia ICM. Each point represents the surface brightness of an annulus with a thickness of 4 arcmin centred in NGC 3268. The dotted line represents the beta model fitted to the data.

of a CC for low-redshift clusters with high-quality data. In addition, they conclude that for higher redshift clusters, the cuspiness of the brightness profile is the best estimator. We estimated t_{cool} for the core of Antlia following Pascut & Ponman (2015). The cooling time is given by

$$t_{cool}(r) = \frac{3}{2} \frac{\mu_e \, n_e \, V \, k_T}{\mu \, L_x}, \tag{1}$$

where k_T and n_e are the gas temperature and electron number density in a spherical shell of volume V at radius r, respectively, and L_x is the luminosity radiated by the shell. We note that equation (1) is equivalent to equation (14) in Hudson et al. (2010). Pascut & Ponman (2015) use standard values for the mean mass per electron (μ_e) and mean mass per particle (μ), assuming a fully ionized plasma with metallicity 0.3 $Z_\odot$. We obtained lower metallicities in the spectral analysis of region A1, but assume $\mu_e = 1.15$ and $\mu = 0.597$, as in Pascut & Ponman (2015), since the differences are not significant.

We consider a shell with inner radius equal to 40 arcsec in order to avoid the emission of NGC 3268 and an outer radius $0.1 R_{500}$, where R_{500} is the radius enclosing a mean density of 500 times the critical density at the system's redshift. In this way, we compute a cooling time representative of the inner region of the cluster. R_{500} was calculated following the relation between temperature and radius proposed by Sun et al. (2009):

$$h E(z) R_{500} = 0.602 \left(\frac{T_{500}}{3 \, keV} \right)^{0.53}, \tag{2}$$

where h is the Hubble parameter and $E(z)$ is the evolution factor, $E(z) = \sqrt{\Omega_M (1 + z)^3 + \Omega_\Lambda}$. We use the temperature obtained by Wong et al. (2016) in the outer regions of Antlia, since the FOV of the *XMM–Newton* observations is too small to contain a significant part of the volume inside R_{500}. They fitted an absorbed plasma model (PHABS∗APEC) and obtained a temperature of $T_x = 1.54$ keV. Applying this value, we obtained $R_{500} = 0.602$ Mpc for the Antlia Cluster, which corresponds to an aperture of 52 arcmin, considering $z = 0.0087$. Thus, the outer radius of the spherical shell spans roughly 4.5 arcmin in the cluster core.

The value of the temperature inside the shell is $k_T = 1.71$ keV. The electron density, n_e, is derived by means of

$$n_e(r) = \sqrt{\frac{(n_e/n_H) \, N_{spec} \, 4\pi [D_a (1 + z)]^2}{V \, 10^{-14}} \frac{\epsilon(r)}{C}}, \tag{3}$$
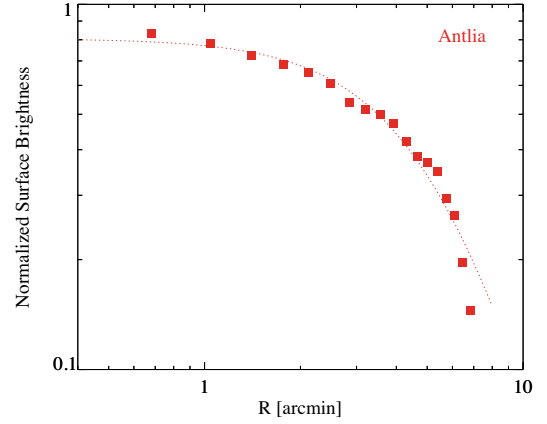
where $\epsilon(r)$ is the counts emissivity integrated over the volume of the shell, and C is the total number of counts from the source within $0.1 R_{500}$. D_a is the angular diameter distance. N_{spec} is the normalization of the thermal model fitted using XSPEC. Following Pascut & Ponman (2015), we computed the emissivity by means of the analytical expression

$$\epsilon(r) = \epsilon_0 [1 + (r/r_c)^2]^{-\eta}, \tag{4}$$

where $\eta = 3\beta$ and $\epsilon_0 = S_0 / [2r_c \int_0^{\pi/2} \cos \alpha^{2(\eta-1)} d\alpha]$. β, S_0, and r_c are free parameters of a beta model fitted to the brightness profile of the cluster.

For this purpose, we constructed a brightness profile of the Antlia Cluster using annuli centred on NGC 3268 and with $\Delta R = 0.25$ arcmin. The brightness profile was constructed using the *Chandra*'s data analysis system (CIAO 4.9 Fruscione; McDowell & Allen 2006). We used an image in the spectral range 0.3–5.keV and masked point-like sources and the SP of emission in the image to avoid brightness excesses. We subtracted the same background used in the spectral analysis. For distances larger than 10 arcmin of the cluster centre, the brightness profile is severely affected because of the background subtraction (see Section 3.4.1). Then, we fitted a beta model to the data given by

$$S(r) = S_0 [1 + (r/r_c)^2]^{-3\beta + 0.5}, \tag{5}$$

where S_0 and r_c are the central surface brightness and core radius, respectively. The fitted values to the brightness profile are $\beta = 0.7$, $r_c = 6.16$ arcmin, and $S_0 = 80.58$. Fig. 12 shows the normalized brightness profile and the best-fitting model with a dotted line.

Using the derived parameters, we estimated a cooling time for the Antlia Cluster central region at $R = 0.1 R_{500}$ of $t_{cool} = 13.6$ Gyr, which is nearly the age of the Universe within our assumed cosmology. Hudson et al. (2010) show the distribution of central cooling times of a sample of nearby clusters and a clear bimodality between strong CC clusters (those with t_{cool} shorter than 1 Gyr) and non-CC clusters (those with t_{cool} longer than roughly 10 Gyr) is present. However, they defined a third population of weak CC clusters with cooling times between 1 and 10 Gyr. Considering the value of t_{cool} estimated at its centre, we can conclude that Antlia Cluster has not even a weak CC as the temperature at the centre could suggest.

4 DISCUSSION

The observation of X-ray emission in galaxy clusters has been a useful tool to derive properties that describe their physical state. Here, we present a detailed analysis of two *XMM–Newton* observations to study the region around NGC 3268 in the Antlia Cluster.

In Section 2.2, we show the images of the region under consideration. A peak of extended emission lies nearly coincident with the position of one of the central galaxies of the Antlia Cluster, NGC 3268. Moreover, an SP of emission is present on the west side. These X-ray sources of emission were already noted by Nakazawa et al. (2000). They used data from the GIS on board the *ASCA* satellite to analyse the core of the Antlia Cluster, but the peak of emission to the west of around NGC 3268 fell in the window-support grids and could not be correctly observed. Therefore, they used data from the PSPC instrument on board the *ROSAT* satellite to determine which of the observed peaks represented the real minimum of the gravitational potential. They argued that the SP was a point-like source. We also detected the SP of emission at ∼4.68 arcmin to the west of the peak associated with NGC 3268. However, our images show that the emission is widely extended and it can hardly be accounted as a point-like source, as also noted by Wong et al. (2016).

We examined optical images of these regions looking for an optical counterpart to understand the nature of this emission, and a combined image of filters *R* and *C* was needed to reveal an extended object in the coordinates of the emission. Despite the low resolution of the optical images, we performed different fits to the brightness profile of the extended object using a Sérsic model and found that the one with a Sérsic index of $n = 3$ reproduces more accurately the brightness profile of the source. Deeper optical images are needed to fully determine the nature of the optical source lying at the centre of the SP of emission and the surrounding sources.

The spectral analysis of the sources provide physical and chemical properties of the emitting plasma. In our spectral analysis of the SP of emission, we found a redshifted Fe emission line. We added a second model APEC to the spectral data, with the redshift as a free parameter. We found that the SP of emission of the ICM is an extended source lying at redshift $z \sim 0.41$. Together with the evidence of the extended object near the centre of emission, which is consistent with an elliptical galaxy, and the presence of several extended objects surrounding it, we can associate it to a cluster of galaxies, although angular resolution limits prevent us from performing a more detailed spatially resolved study of its physical properties. Wong et al. (2016) also suggested that this emission is likely a cluster of galaxies.

The result of the temperature in region A0 of the cluster shown in Section 3 is consistent within the errors with the measurements using the *ASCA* satellite by Nakazawa et al. (2000), who found a constant temperature of 2.0 keV for the gas within 22 arcmin around NGC 3268. We found that the inclusion of a power-law component is needed to correctly fit the more energetic part of the spectrum at the centre region surrounding NGC 3268, tagged as A0. With the inclusion of the power law, the thermal model used to account for the thermal contribution of the spectrum fits the observations with a temperature of $k_T = 1.32$ keV.

The Antlia Cluster is usually considered as a non-CC cluster. However, the temperature of the thermal plasma obtained in Section 3, in a small region around the centre of the cluster, shows a slight drop relative to the surrounding ICM. This could suggest the presence of a weak CC in Antlia. In Section 3.5, we estimated the cooling time out to radius $0.1\,R_{500}$ and obtained $t_{cool} = 13.6$ Gyr.

These results confirm the status of non-CC of the Antlia Cluster. The geometrical configuration of the intra-cluster gas of this dynamically active cluster provides hints that indicate that the cluster centre, surrounding NGC 3268, could be facing an ongoing process of merger with substructures falling inwards, as suggested by Hess et al. (2015), and/or that it has a relatively recent and rich merger history, also supported by the lack of a CC, confirmed in this work.

Another interesting feature in the ICM of Antlia is a wall-like feature (region SR) to the east of the galaxy, reported in Section 2 and analysed spectroscopically in Section 3. We showed that this structure has a lower temperature than that of the surrounding ICM.

Dedicated observations of the background cluster (named as the SP of emission throughout this paper) performed with the *Chandra* X-ray Observatory are necessary, given its high spatial and spectral resolution, to construct detailed temperature and pressure maps of the region in order to characterize the cluster in more detail.

REFERENCES

Abell G. O., Corwin H. G.,, Jr, Olowin R. P., 1989, ApJS, 70, 1
Anders E., Grevesse N., 1989, GCA, 53, 197
Arnaud K. A., 1996, in Jacoby G. H., Barnes J., eds, ASP Conf. Ser. Vol 101, Astronomical Data Analysis Software and Systems V. Astron. Soc. Pac., San Francisco, p. 17
Balucinska-Church M., McCammon D., 1992, ApJ, 400, 699
Bassino L. P., Richtler T., Dirsch B., 2008, MNRAS, 386, 1145
Calderón J. P., Bassino L. P., Cellone S. A., Richtler T., Caso J. P., Gómez M., 2015, MNRAS, 451, 791
Caso J. P., Richtler T., 2015, A&A, 584, A125
Caso J. P., Bassino L. P., Richtler T., Smith Castelli A. V., Faifer F. R., 2013, MNRAS, 430, 1088
Caso J. P., Bassino L. P., Richtler T., Calderón J. P., Smith Castelli A. V., 2014, MNRAS, 442, 891
Cavagnolo K. W., Donahue M., Voit G. M., Sun M., 2009, ApJS, 182, 12
Dirsch B., Richtler T., Bassino L. P., 2003, A&A, 408, 929
Edge A. C., Stewart G. C., Fabian A. C., 1992, MNRAS, 258, 177
Ferguson H. C., Sandage A., 1990, AJ, 100, 1
Ferguson H. C., Sandage A., 1991, AJ, 101, 765
Fruscione A., McDowell J. C., Allen G. E. e. a., 2006, in SPIE Conf. Ser. p. 62701V
Harris W. E., Whitmore B. C., Karakla D., Okoń W., Baum W. A., Hanes D. A., Kavelaars J. J., 2006, ApJ, 636, 90
Hess K. M., Jarrett T. H., Carignan C., Passmoor S. S., Goedhart S., 2015, MNRAS, 452, 1617

Hopp U., Materne J., 1985, A&AS, 61, 93

Hudson D. S., Mittal R., Reiprich T. H., Nulsen P. E. J., Andernach H., Sarazin C. L., 2010, A&A, 513, A37

Jørgensen I., Chiboucas K., 2013, AJ, 145, 77

Kalberla P. M. W., Burton W. B., Hartmann D., Arnal E. M., Bajaja E., Morras R., Pöppel W. G. L., 2005, A&A, 440, 775

Kormendy J., Fisher D. B., Cornell M. E., Bender R., 2009, ApJS, 182, 216

Larsen S. S., 1999, A&AS, 139, 393

Mauch T., Murphy T., Buttery H. J., Curran J., Hunstead R. W., Piestrzynski B., Robertson J. G., Sadler E. M., 2003, MNRAS, 342, 1117

Maughan B. J., Giles P. A., Randall S. W., Jones C., Forman W. R., 2012, MNRAS, 421, 1583

Miceli M., Bamba A., Orlando S., Zhou P., Safi-Harb S., Chen Y., Bocchino F., 2017, A&A, 599, A45

Mittal R., Hudson D. S., Reiprich T. H., Clarke T., 2009, A&A, 501, 835

Nakazawa K., Makishima K., Fukazawa Y., Tamura T., 2000, PASJ, 52, 623

Oldham L. J., Houghton R. C. W., Davies R. L., 2017, MNRAS, 465, 2101

Pascut A., Ponman T. J., 2015, MNRAS, 447, 3723

Pedersen K., Yoshii Y., Sommer-Larsen J., 1997, ApJ, 485, L17

Planck Collaboration XIII, 2016, A&A, 594, A13

Reiprich T. H., Böhringer H., 2002, ApJ, 567, 716

Sersic J. L., 1968, Atlas de galaxias australes. Observatorio Astronomico, Cordoba, Argentina

Smith R. K., Brickhouse N. S., Liedahl D. A., Raymond J. C., 2001, ApJ, 556, L91

Smith Castelli A. V., Faifer F. R., Richtler T., Bassino L. P., 2008, MNRAS, 391, 685

Smith Castelli A. V., Cellone S. A., Faifer F. R., Bassino L. P., Richtler T., Romero G. A., Calderón J. P., Caso J. P., 2012, MNRAS, 419, 2472

Sun M., Voit G. M., Donahue M., Jones C., Forman W., Vikhlinin A., 2009, ApJ, 693, 1142

Sweet S. M. et al., 2017, MNRAS, 464, 2910

Wong K.-W., Irwin J. A., Wik D. R., Sun M., Sarazin C. L., Fujita Y., Reiprich T. H., 2016, ApJ, 829, 49

This paper has been typeset from a TEX/LATEX file prepared by the author.